

Weighted diffraction-based migration velocity analysis of common-offset GPR reflection data

Yu Liu, James Irving, and Klaus Holliger

Abstract—Migration focusing analysis of diffractions is an increasingly important tool for estimating the large-scale subsurface velocity structure from surface-based common-offset ground-penetrating radar (GPR) reflection data. We present a weighting strategy whose aim is to improve the reliability of estimations of the root-mean-square (RMS) velocity obtained using a local semblance focusing measure. In this regard, we increase the resolution of the inferred semblance spectra through a weighting function that varies in accordance with the sensitivity of a diffraction curve to changes in velocity. The weighting function is derived from coherency and slope attributes of the diffracted wavefield components. To demonstrate the viability of our proposed method, we consider its application in two synthetic test cases and one field GPR dataset. Compared with conventional unweighted local semblance spectra, their weighted counterparts allow for a significantly increased resolution and correspondingly reduced picking uncertainty.

Index Terms—GPR, diffraction, velocity analysis, migration, attribute analysis.

I. INTRODUCTION

ESTIMATING a reliable model of the velocity distribution in the subsurface is a critical step of the seismic and ground-penetrating radar (GPR) reflection processing and imaging workflows. Among the various methods available, diffraction-based velocity analysis is particularly useful when no offset-dependent information is available, as is notably the case for typical surface-based GPR reflection measurements acquired using a single bistatic, common-offset transmitter-receiver antenna configuration [1], [2].

There are generally three approaches available to infer the subsurface velocity structure based on diffractions, all of which originated in seismic data processing. The first one involves migration focusing analysis of diffraction events. Since a diffraction migrated with the correct velocity will collapse to a point at its apex, Harlan et al. [3] proposed to remove reflections from the data and to estimate the velocity structure through an evaluation of diffraction focusing as a function of different migration velocities. In this regard, Fomel et al. [4] performed diffraction separation using the so-called plane-wave destruction method and evaluated diffraction focusing based on velocity continuation and local kurtosis techniques. Burnett and Fomel [5] extended this procedure for 3D azimuthally anisotropic velocity analysis, whereas Decker et al. [6] further

decomposed the diffractions into slope components and estimated the velocity based on the local diffraction semblance. The second approach for diffraction-based velocity analysis is to examine diffraction events in the post-migration dip-angle domain. In dip-angle common image gathers, specular reflections appear as hyperbolic events centered at the reflector dip and curving upward, even when over- or under-migrated. Conversely, diffractions will be flat in this domain when using the correct migration velocity, or curve upward or downward in the case of over- and under-migration, respectively. Based on this feature, Reshef and Landa [7] performed migration velocity analysis in the dip-angle domain by measuring diffraction flatness. Klovov and Fomel [8] further proposed the use of the hybrid Radon transform to improve diffraction separation and velocity analysis in the dip-angle domain. Finally, the third approach for diffraction-based velocity analysis is to perform diffraction wavefront tomography. Based on the idea that the wavefront attributes together with traveltimes can be used to locally approximate the kinematic response of reflection points [9], Bauer et al. [10] performed ray-based tomographic inversion for zero-offset seismic data, where wavefront attributes were extracted directly from the diffraction section. Recently, Preine et al. [11] applied diffraction wavefront tomography to single-channel marine seismic data acquired in a volcanic environment.

Arguably, migration focusing analysis is the most commonly used method of diffraction-based velocity analysis for common-offset GPR data [12]–[16]. In this regard, diffraction semblance has proven to be an effective focusing indicator [17]. Diffraction semblance can be regarded as the normalized squared correlation of the diffracted event with a constant [18]. This inherently assumes that there is no amplitude or phase variation along the hyperbolic trajectory. When this assumption is violated, for example due to the effects of attenuation or the presence of noise, diffraction semblance may no longer provide robust velocity estimates. A similar problem exists in classic common mid-point (CMP) velocity analysis, where semblance is computed along flattened reflection hyperbolae [19] and becomes less robust in the presence of strong variations in reflection amplitude. In the latter case, the problem was addressed by introducing semblance weighting terms [20], [21], which allow for an improvement in the resolution of CMP-based velocity spectra by placing more weight on data that are more sensitive to changes in velocity in the semblance

calculation.

In this paper, we develop a diffraction semblance weighting function in order to enhance diffraction-based velocity analysis for common-offset GPR reflection data. Linear coherency analysis [22], [23] is used to estimate the local slopes and coherencies of the diffracted wavefield components, which in turn are used to derive the weights. We begin by presenting the methodological background of our approach. We then assess the viability of the proposed technique by testing it on two synthetic common-offset GPR data examples. Finally, the method is applied to a field GPR dataset from a typical surficial alluvial environment, where borehole logs are available to assess the results obtained.

II. METHODOLOGY

Our diffraction velocity analysis procedure begins with the separation of the diffracted wavefield from the common-offset GPR data. To this end, we employ plane-wave destruction (PWD) filtering [24], [25] to eliminate the specular reflections. This is accomplished using the programs ‘sfdip’ and ‘sfpwd’ in Madagascar (<https://reproducibility.org/>), an open-source data analysis package. Once the diffracted wavefield has been isolated, the data are ready for migration focusing analysis to estimate the corresponding root-mean-square (RMS) velocity structure.

Migration focusing of diffractions can be measured by the diffraction semblance, which is defined as

$$s(t, x, v) = \frac{\{F_v[a(t, x)]\}^2}{F_v[a^2(t, x)]}, \quad (1)$$

where $a(t, x)$ is the amplitude of the diffracted wavefield with t and x denoting the time and space coordinates, respectively, and F_v the time migration operator for a constant velocity v . Diffraction semblance is a normalized coherency measure performed along a hyperbolic trajectory. More generally, we can consider the weighted diffraction semblance, which is defined as

$$s_w(t, x, v) = \frac{\{F_v[a(t, x)w(t, x)]\}^2}{F_v[a^2(t, x)]F_v[w^2(t, x)]}. \quad (2)$$

The weighted semblance can be regarded as the squared correlation between the diffracted wavefield and the weighting function $w(t, x)$. When $w(t, x)$ is equal to a constant, (2) is equivalent to (1).

For CMP-type seismic velocity analysis, Luo and Hale [20] showed that the use of a weighted semblance function, where greater emphasis is placed on parts of the normal moveout (NMO) curve that are particularly sensitive to velocity changes, can significantly increase the resolution of the velocity spectra obtained. To improve the resolution of diffraction velocity analysis for common-offset GPR data, we similarly aim to develop a weighting function, to be used in (2), that places more emphasis on parts of the diffraction curve that have greater sensitivity to changes in the migration velocity. To this end, we consider a point diffractor whose apex appears on a GPR section at the two-way traveltime τ (Fig. 1). Assuming that the diffractor is embedded in a homogeneous medium having a value of the squared slowness of $\gamma = 1/v^2$, the traveltime of

the diffraction curve in terms of the zero-offset traveltime is approximately given by

$$t = \sqrt{\tau^2 + 4\gamma x_d^2}, \quad (3)$$

where x_d denotes the horizontal distance between the diffraction apex and the observation location at the surface. Taking the derivative of (3) with respect to the squared slowness, we arrive at

$$\frac{\partial t}{\partial \gamma} = \frac{2x_d^2}{\sqrt{\tau^2 + 4\gamma x_d^2}} = \frac{2x_d^2}{t}. \quad (4)$$

We see from (4) that the change in traveltime along the diffraction hyperbola that results from a change in the squared slowness is proportional to the horizontal distance from the apex squared and inversely proportional to the traveltime. The distance x_d can be expressed in terms of the local slope p of the diffraction curve, which is equal to the derivative of (3) with respect to x_d . Taking $\partial t/\partial x_d$, solving for x_d , and substituting the result into (4) yields

$$\frac{\partial t}{\partial \gamma} = \frac{tp^2}{8\gamma^2}. \quad (5)$$

Equation (5) suggests that our weighting function for diffraction semblance should vary proportionally to the product of the traveltime and the squared local slope of the diffracted wavefield. To estimate the latter, we perform so-called C2 coherency analysis, where we seek to find the value of p that maximizes a linear semblance measure over a particular time and trace window [23]

$$\max_p \frac{1}{n} \frac{\sum_{\delta t} \{\sum_{i=1}^n a[t_0 + p(\Delta x_i), x_0 + \Delta x_i]\}^2}{\sum_{\delta t} \sum_{i=1}^n a^2[t_0 + p(\Delta x_i), x_0 + \Delta x_i]}, \quad (6)$$

where δt represents the interval over which vertical summation is performed, n is the number of considered neighboring traces, position (t_0, x_0) is where the slope p is estimated, and Δx_i denotes the horizontal distance from position (t_0, x_0) . The C2 coherency analysis procedure based on (6) yields not only a slope attribute $p(t, x)$, but also a maximum-semblance-based coherency attribute $c(t, x)$. For parasitic slopes related to random noise, this coherency value will be small because of the inherent lack of continuity. Conversely, for the diffracted parts of the wavefield, the coherency attribute will take on a high value, even in the case of weak amplitudes, because the hyperbolae can be locally approximated by continuous linear events.

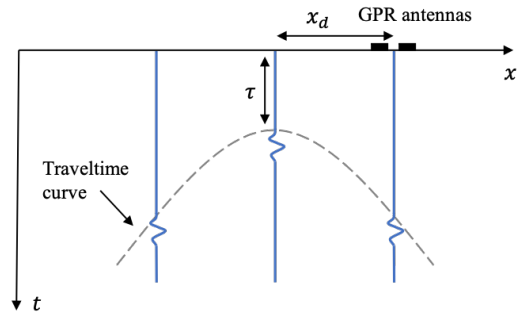


Fig. 1. Schematic illustration of a diffraction whose apex appears at two-way traveltime τ in a common-offset GPR section. x_d denotes the horizontal distance between the considered observation point at the surface and the diffraction apex.

To formulate our weighting function for diffraction semblance velocity analysis, which must be defined everywhere across the diffraction section, we first evaluate (5) using the local slope estimate derived from the C2 coherency analysis procedure described by (6). Next, to avoid the consideration of regions that do not correspond to coherent diffraction events, we set to zero all parts of the section where the estimated coherency value is below a chosen threshold c_0 , which is determined empirically. This masking procedure can be expressed mathematically as

$$u(t, x) = f(t, x) \cdot H[c(t, x) - c_0], \quad (7)$$

where $u(t, x)$ denotes the masked data, $f(t, x)$ the results of (5), and H the Heaviside step function. Finally, we tailor our weight function $w(t, x)$ such that we can easily control the degree of weighting of diffraction events based on (5). This is done by normalizing $u(t, x)$ by its maximum value u_{max} and introducing the balance parameter λ , which can take on values between 0 and 1

$$w(t, x) = 1 - \lambda + \lambda \left[\frac{u(t, x)}{u_{max}} \right]. \quad (8)$$

When $\lambda = 0$, we see that $w(t, x) = 1$, meaning that the weighted semblance in (2) is equivalent to the normal semblance described by (1). Conversely, when $\lambda = 1$, the weighting is based entirely on the sensitivity relationship expressed by (5).

To perform the diffraction semblance velocity analysis, (2) is evaluated over a suite of velocity values. This yields a t - x - v cube of weighted diffraction semblance values. Using the automatic picking program 'sfpick' in Madagascar [18], the maxima on each t - v panel are selected and a 2D RMS velocity model is generated. This result, if desired, can then be transformed to a corresponding interval velocity model using the constrained Dix inversion program 'sfdix' [26]. The flowchart in Fig. 2 illustrates the essential elements of our proposed approach.

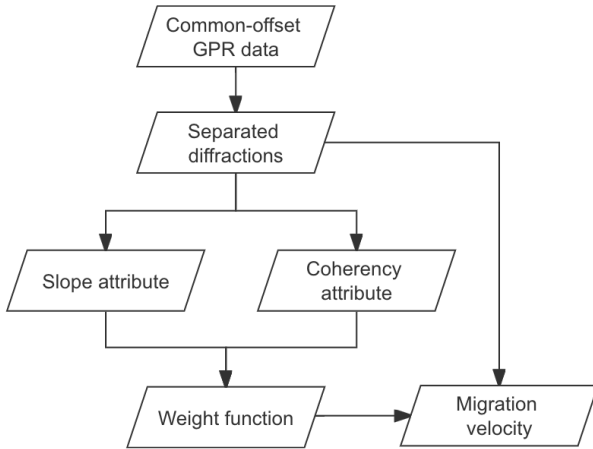


Fig. 2. Flowchart illustrating the essential elements of the proposed diffraction semblance weighting strategy for estimating the subsurface migration velocity structure from surface-based common-offset GPR reflection data.

A. Vertical gradient model

We first show the application of our diffraction velocity analysis strategy to a synthetic example characterized by a negative velocity gradient with depth, which is commonly encountered in surficial environments in response to a gradual increase of the soil water content (Fig. 3a). Ten point-type diffractors are distributed randomly throughout this model, for which we generated synthetic common-offset GPR reflection data using the gprMax software [27], which solves Maxwell's equations using the finite-difference time-domain (FDTD) method. The subsurface dielectric permittivity ϵ is assumed to be frequency-independent and is obtained from the GPR velocity v using the low-loss approximation $v \approx 1/\sqrt{\epsilon\mu}$ [28]. The magnetic permeability μ is assumed to be equal to its value in free space, and the electrical conductivity is fixed at a constant value of 1 mS/m. The source current is defined as Ricker wavelet having a dominant frequency of 200 MHz which, in turn, results in a propagating electromagnetic pulse corresponding to the first derivative. The distance between the transmitter and receiver antennas is set to 0.5 m and traces are simulated every 0.1 m along the survey profile. The fact that the antenna offset is not strictly zero leads to an inherent underestimation of the velocity that decreases with increasing depth. For the standard antenna offsets used in surface-based bistatic GPR reflection surveys, the resulting errors can be generally regarded as negligible from a practical point of view.

The resulting synthetic GPR data are contaminated with 5% Gaussian random noise with regard to the maximum absolute amplitude below the direct wave, and are subjected to a standard signal processing sequence consisting of (i) amplitude scaling to compensate for energy spreading, absorption, and scattering using a gain function consisting of a linear and an exponential part; (ii) elimination of the direct air and ground arrivals by subtracting the average trace calculated over a time window from 0 to 25 ns; and (iii) 20-600 MHz bandpass filtering. Fig. 3b shows the raw noise-contaminated GPR data after amplitude scaling only. Fig. 4a then illustrates the final processed GPR data, which, due to the absence of reflecting interfaces in the underlying velocity model, only consist of diffractions and noise.

We next performed C2 coherency analysis described by (6) on the processed GPR data, which leads to the local coherency and slope attribute sections shown in Figs. 4b and 4c, respectively. We see that the estimated coherencies are strong for the diffractions and rather weak and disorganized for the noise, which allows us to easily identify the diffractions and estimate their slopes. Based on this information, (5), (7) and (8) are used to calculate the semblance weighting function to be used in diffraction velocity analysis, where balance parameter λ is set to a value of 0.5 (Fig. 4d). Through empirical testing, we have found that intermediate values of λ lead to the best results in the velocity spectra, and, for consistency, we therefore consider $\lambda = 0.5$ for all of the examples presented in the manuscript. The weights are seen to increase with distance from the apex of each diffraction hyperbola, as the diffraction curves

have a greater sensitivity to changes in velocity in these locations.

We compute both the unweighted and weighted local semblance based on (1) and (2) for a suite of velocity values ranging from 0.07 m/ns to 0.13 m/ns. The corresponding velocity spectra for lateral positions of 3, 9, 15, 21 and 27 m are shown in Fig. 5. Note that the velocity resolution for the weighted panels is significantly higher than that for the unweighted panels, thanks to a heavier emphasis in the semblance calculation on parts of the diffraction hyperbolae that are most sensitive to velocity changes. The weighted panels are clearly more amenable to velocity picking, particularly if done manually. In Fig. 6a, we show the derived 2D RMS velocity structure for the entire GPR section, which was obtained by automatically picking the maxima on the time-velocity panels for all trace locations considering an average velocity at the surface of 0.12 m/ns. The impact of using different velocities in the immediate subsurface on automatic picking has been investigated by [2]. In practice, the surficial velocity can be rather easily and reliably estimated based on the linear moveout of the direct ground wave as a function of antenna offset. The result in Fig. 6a agrees well with the true RMS velocity structure of the vertical gradient model, which is presented in Fig. 6b. This indicates that the inherent velocity bias related to the non-zero antenna offset of surface-based bistatic GPR reflection surveys is, as mentioned above, unlikely to be of any practical significance. Fig. 6c shows the corresponding depth-converted interval velocity model, which was obtained via Dix inversion. We see that the derived velocity field is largely consistent with the underlying gradient model (Fig. 3a). The discrepancy in the lower part of the profile is related to the relative scarcity of complete diffraction hyperbolae in this part of the synthetic data. Finally, Fig. 6d shows the migrated GPR image in the depth domain, which was obtained by first performing Kirchhoff time migration using the estimated RMS velocity structure, and then converting from time to depth based on the corresponding interval velocities. We see that the diffraction hyperbolae have collapsed effectively into their apexes whose positions are consistent with those in the underlying model (Fig. 3a).

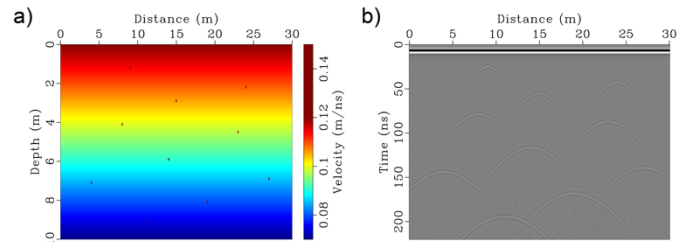


Fig. 3. a) Velocity model characterized by a negative velocity-depth gradient. Ten point-type diffractors are distributed randomly throughout the model. b) Corresponding synthetic common-offset GPR reflection data with 5% Gaussian random noise added.

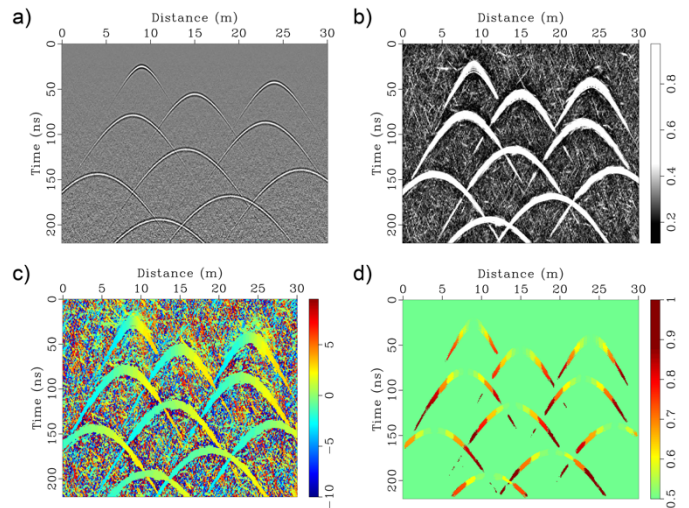


Fig. 4. Diffraction semblance weight function calculation for the vertical gradient velocity model example presented in Fig. 3. a) Synthetic common-offset GPR data from Fig. 3a after processing. b) Corresponding coherency attribute. c) Corresponding slope attribute. d) Inferred weights for diffraction velocity analysis.

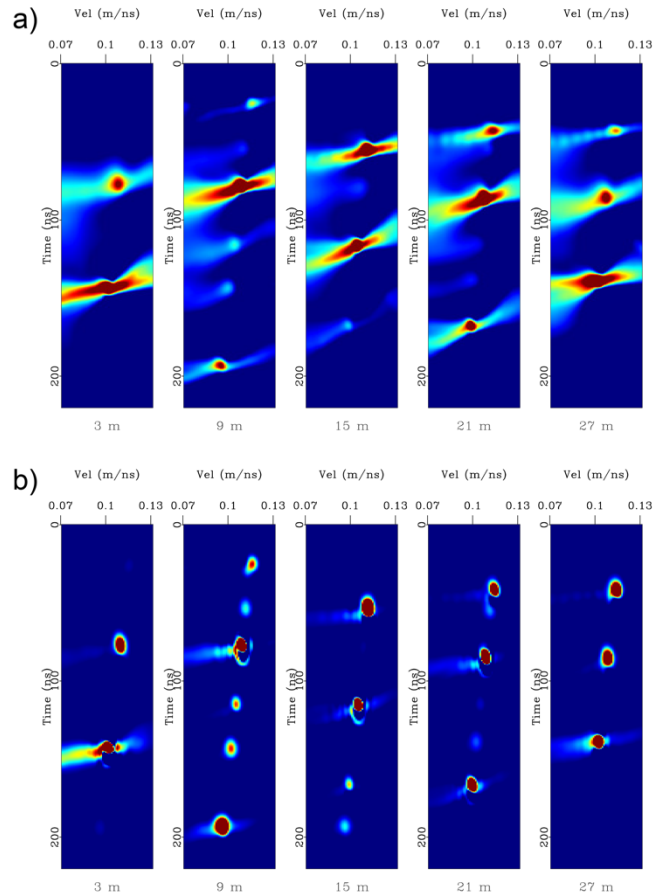


Fig. 5. a) Unweighted and b) weighted diffraction semblance spectra inferred for the vertical gradient velocity model example at lateral distances of 3, 9, 15, 21, and 27 m.

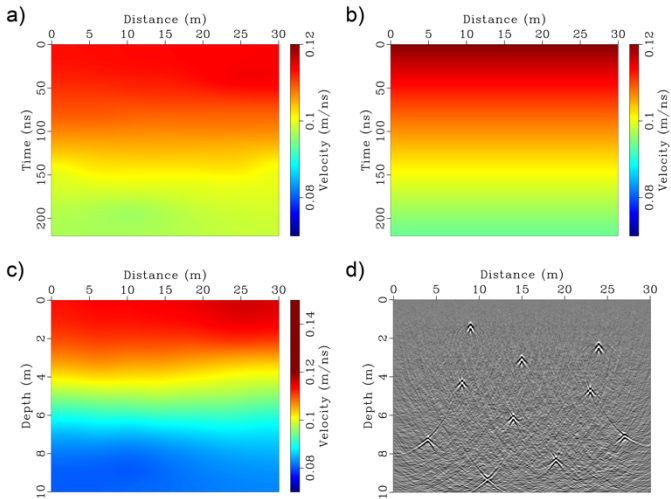


Fig. 6. a) Estimated and b) true RMS velocity distribution for the vertical gradient velocity model example (Fig. 3a). c) Estimated interval velocity model obtained by Dix inversion. d) Corresponding migrated depth image of the common-offset GPR data (Fig. 3b).

B. Layered model

Our second synthetic example, presented in Fig. 7a, is based upon a layered velocity model and is similar to the example considered by Yuan et al. [2] in a recent GPR diffraction velocity analysis study. The model has two major units of constant velocity, which are separated by a dipping interface. Each of the two constant velocity units contains three diffractors. A thin horizontal layer is also present in the lower part of the second unit. As before, we simulated a common-offset GPR reflection survey, assuming low-loss conditions for the conversion of velocity to dielectric permittivity and using a constant electrical conductivity of 1 mS/m and a magnetic permeability equal to its value in free space. The gprMax FDTD software was again used to perform the GPR simulations with a Ricker wavelet having a dominant frequency of 200 MHz as the source current function, a transmitter-receiver spacing of 0.5 m, and a lateral trace increment of 0.1 m. After contaminating the resulting data with 5% Gaussian random noise with regard to the maximum absolute amplitude below the direct wave, they were subjected to the same signal processing sequence as described previously. Fig. 7b shows the raw noise-contaminated GPR data after amplitude scaling only, where we observe that, in addition to the diffraction hyperbolae arising from the point-type scatterers, specular reflections corresponding to the layer boundaries are present.

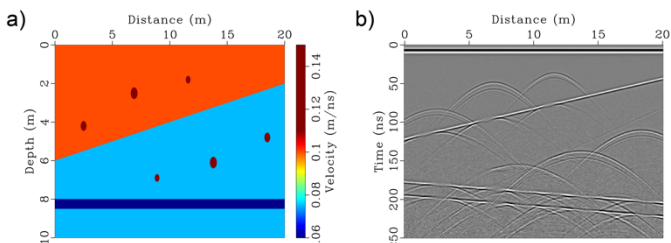


Fig. 7. a) Layered velocity model containing six point-type diffractors. b) Corresponding synthetic common-offset GPR reflection data with 5% Gaussian random noise added.

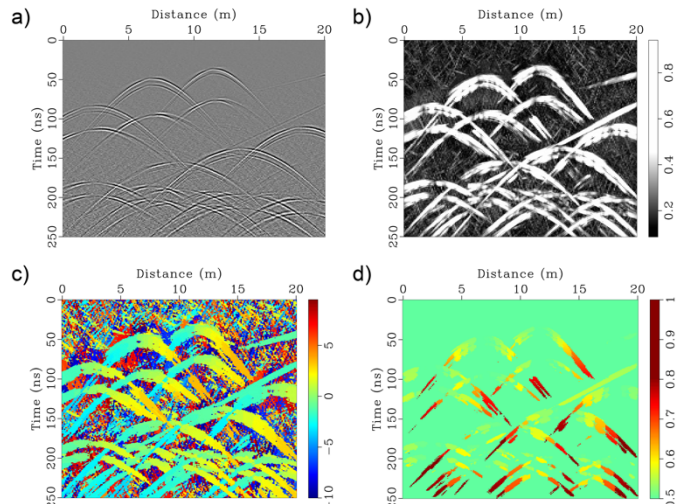


Fig. 8. Diffraction semblance weight function calculation for the layered velocity model example presented in Fig. 7. a) Synthetic common-offset GPR data from Fig. 7b after processing and diffraction separation. b) Corresponding coherency attribute. c) Corresponding slope attribute. d) Inferred weights for diffraction velocity analysis.

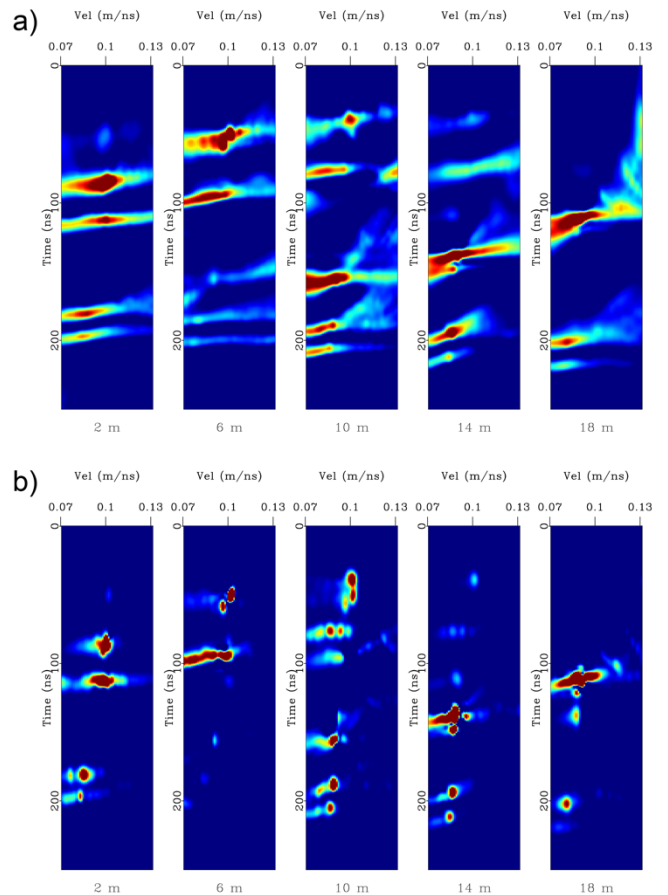


Fig. 9. a) Unweighted and b) weighted diffraction semblance spectra inferred for the layered velocity model example at lateral distances of 2, 6, 10, 14, and 18 m.

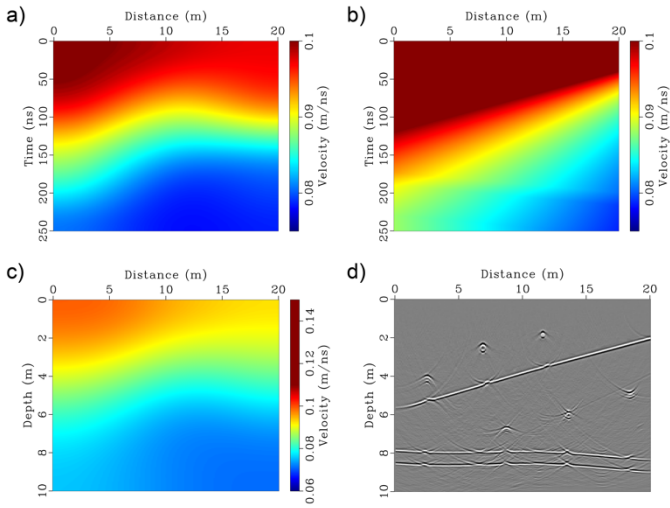


Fig. 10. a) Estimated and b) true RMS velocity distribution for the layered velocity model example (Fig. 7a). c) Estimated interval velocity model obtained by Dix inversion. d) Corresponding migrated depth image of the common-offset GPR data (Fig. 7b).

As the data in Fig. 7b contain both reflections and diffractions, we applied PWD filtering after processing in order to eliminate the specular reflections. Fig. 8a shows the result, where we see that the diffractions have been preserved and that the reflections have been largely eliminated. In Figs. 8b and 8c, we show the local coherency and slope attributes corresponding to the diffracted wavefield in Fig. 8a, respectively. In Fig. 8d, we show the weight function calculated from these attributes based on (5), (7) and (8), where balance parameter λ was again set to a value of 0.5. As before, we computed both the unweighted and weighted local semblance for a suite of velocity values ranging from 0.07 m/ns to 0.13 m/ns. The corresponding velocity spectra for lateral positions of 2, 6, 10, 14 and 18 m are shown in Fig. 9. Consistent with the results presented previously, the weighted semblance panels are seen to have a considerably higher resolution along the velocity axis and contain fewer artifacts than their unweighted counterparts.

Using automatic velocity picking on all of the weighted semblance panels assuming an average velocity at the surface of 0.1 m/ns, the 2D RMS velocity model presented in Fig. 10a is generated. This result compares reasonably well with true RMS velocity structure of the layered model, which is presented in Fig. 10b. The estimated RMS velocity structure was then used to estimate interval velocities in the time domain through Dix inversion (Fig. 10c). Finally, Fig. 10d shows the corresponding depth image of the GPR data. From this depth image, we see that the position of dipping interface is imaged satisfactorily, that the diffracted parts of the wavefield have been well focused, and that the thin layer is well resolved with its geometric characteristics closely emulating those of the underlying model with the exception of a mild pull-down towards the right-hand side. The latter results from errors in the estimation of the RMS and interval velocity distributions in the overlying part of the model due the relative scarcity of diffractors. Compared to the migrated images of Yuan et al. [2], the positioning of the prevailing structures has been significantly improved.

IV. FIELD DATA EXAMPLE

We now consider the application of our proposed methodology to constant-offset GPR reflection data acquired at the Boise Hydrogeophysical Research Site (BHRS), which is located on a gravel bar adjacent to the Boise River near Boise, Idaho, USA (Fig. 11). The corresponding aquifer is unconfined and consists predominantly of late Quaternary fluvial deposits dominated by gravel and sand. The groundwater table is, with some seasonal variations, located around 2 m depth. A layer of red clay at approximately 18 m depth acts as an aquitard and forms the base of the aquifer [29]. Over the past two decades, a wide range of geophysical and hydrogeological studies have been conducted at the site [30], [31].

The considered GPR data are from an inline profile acquired in 1998 during a 3D survey at the BHRS using a PulseEKKO IV system (Sensors & Software Inc.) with a nominal antenna frequency of 200 MHz. The 30-m-long survey line crosses three boreholes, B5, A1, and B2, where neutron-neutron porosity logs are available below the groundwater table, which was located at a depth of ~ 2.8 m at the time of the survey. The spacing between the transmitter and receiver antennas was set to 0.5 m and traces were acquired every 0.1 m along the profile. The corresponding time sampling interval was 0.8 ns, and 32 stacks were performed at each trace location in order to improve the signal-to-noise ratio.

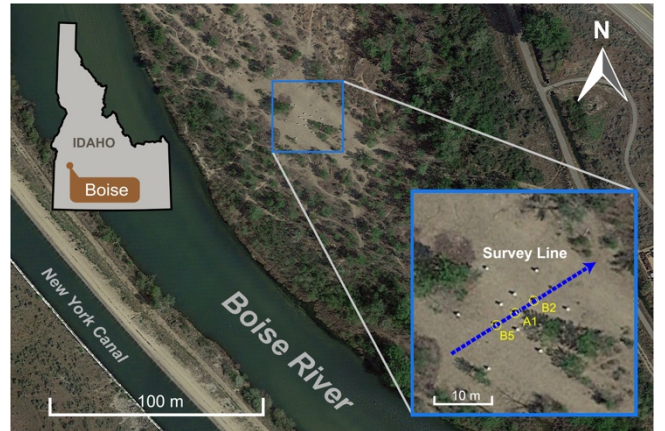


Fig. 11. Map of the BHRS showing the location of the considered common-offset GPR reflection profile (blue dashed line). The profile is aligned with boreholes B5, A1, and B2 (yellow circles).

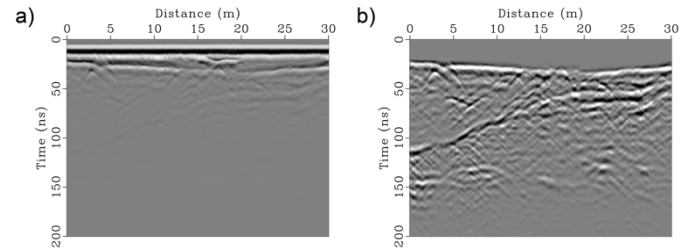


Fig. 12. a) Raw and b) processed common-offset GPR reflection data from the BHRS.

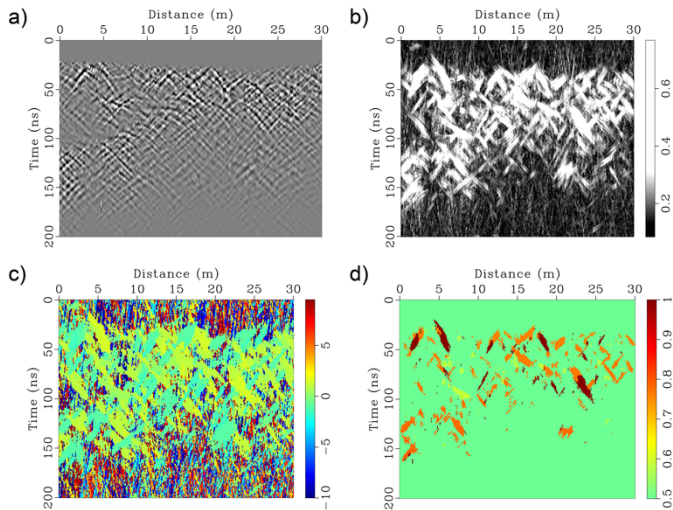


Fig. 13. Diffraction semblance weight function calculation for the common-offset field GPR reflection data from the BHRS. a) Diffracted wavefield obtained from the processed data shown in Fig. 12b. b) Corresponding coherency attribute. c) Corresponding slope attribute. d) Inferred weights for diffraction velocity analysis.

Fig. 12a shows the raw BHRS GPR reflection data. These data were subjected to a typical signal processing flow consisting of time-zero correction, “de-wow” filtering, surgical mute of the direct air and ground arrivals, and amplitude scaling using a gain function consisting of a linear and an exponential part (Fig. 12b). Next, we applied PWD filtering to isolate the diffracted part of the recorded wavefield (Fig. 13a). Though not evident in the original data after standard processing, diffractions do indeed turn out to be quite abundant after wavefield separation.

In Figs. 13b and 13c, we show the local coherency and slope attributes corresponding to the diffracted wavefield shown in Fig. 13a. Fig. 13d shows the weight function calculated for diffraction velocity analysis, where balance parameter λ was again set to 0.5. We computed both the unweighted and weighted local semblance for a suite of velocity values ranging from 0.07 m/ns to 0.13 m/ns. The corresponding velocity spectra for lateral positions of 3, 9, 15, 21 and 27 m are shown in Fig. 14. As for the synthetic test cases, we see that the velocity resolution in the weighted panels shows distinct improvements compared to the unweighted panels and that the uncertainties in velocity picking are decreased by the proposed approach. The corresponding estimated 2D RMS velocity structure is shown in Fig. 15a. Through Dix inversion and time-to-depth conversion, we then obtained the interval velocity model shown in Fig. 15b. Quite interestingly, this smooth, large-scale, diffraction-based velocity model clearly senses the change in water content associated with transition from the vadose zone to the saturated zone at the BHRS. Fig. 15c shows the corresponding depth image of migrated GPR data.

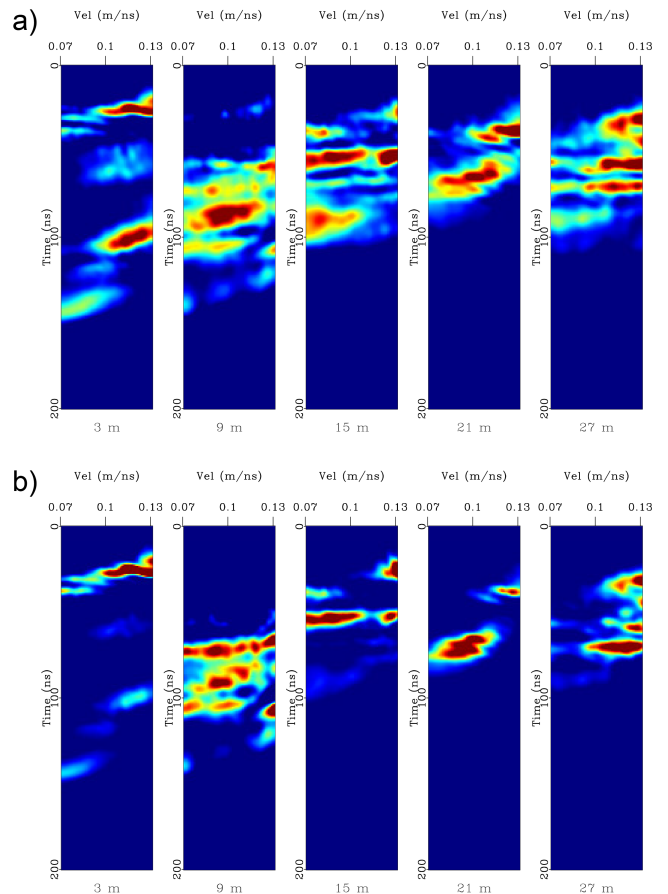


Fig. 14. a) Unweighted and b) weighted diffraction semblance spectra obtained from the BHRS field data at lateral distances of 3, 9, 15, 21, and 27 m.

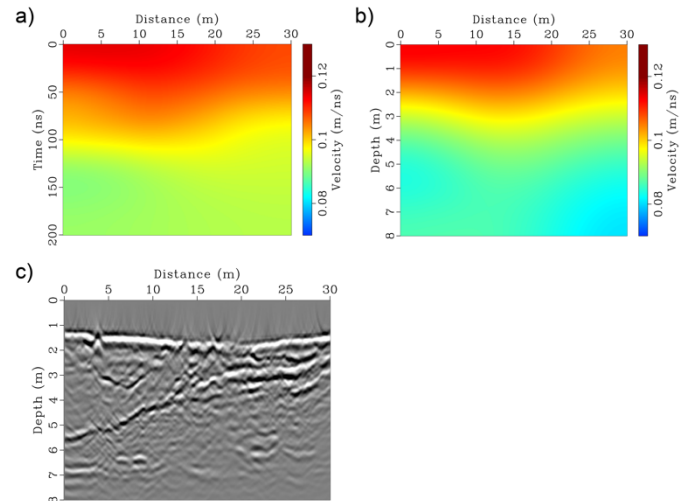


Fig. 15. a) RMS velocity structure estimated from the BHRS field data. b) Estimated interval velocity model obtained by Dix inversion. c) Corresponding migrated depth image of the BHRS field data (Fig. 12b).

To further assess these results, we compare the inferred interval velocity structure with the neutron-neutron porosity logs, which were acquired only within the water-saturated zone, at the borehole locations B5, A1, and B2 (Fig. 16). To this end, we convert the logged porosities to GPR velocity using a

common petrophysical mixing model for the water-saturated part of subsurface [32]

$$v = \frac{c}{\sqrt{\varepsilon_r^s(1-\phi) + \varepsilon_r^w\phi}}, \quad (9)$$

where $c = 0.3$ m/ns is the speed of light in free space, ϕ is the porosity, and $\varepsilon_r^s = 4.6$ and $\varepsilon_r^w = 80$ are the relative dielectric permittivities of the dry solid matrix and water, respectively. Fig. 16 shows the comparison between the estimated and logged velocities at the three borehole locations, which is overall quite favorable.

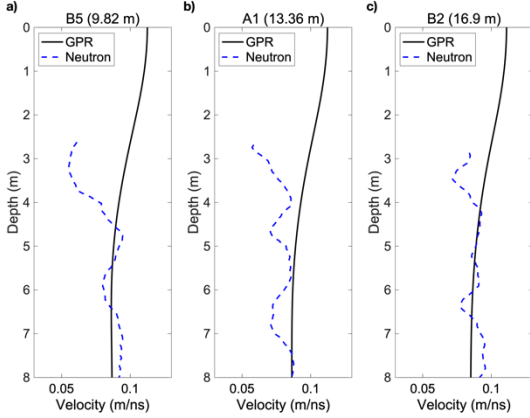


Fig. 16. Comparison of the velocity profiles estimated from GPR diffraction analysis (black solid lines) at the borehole locations a) B5, b) A1, and c) B2 (Fig. 11c) with the corresponding velocity profiles inferred from the neutron-neutron porosity logs acquired within the water-saturated zone (blue dashed lines).

V. DISCUSSION AND CONCLUSIONS

We have presented in this paper a weighting strategy to improve the performance of diffraction-based velocity analysis of surface-based common-offset GPR reflection data using local semblance as the focusing measure. Our weighting function is calculated throughout the GPR section from coherency and slope attributes that are derived from linear coherency analysis of the diffracted wavefield. Through its use, far-distance components of diffraction hyperbolae, whose positions are particularly sensitive to the prevailing RMS velocity, are favoured. This leads to increased focusing and resolution of the resulting semblance spectra, which correspondingly reduces the uncertainties for velocity picking. Tests on synthetic common-offset GPR reflection data for two canonical models and subsequent application to field data corroborate the viability of the proposed weighting method.

Our weight function is designed in an analogous manner to that of Luo and Hale [20], who estimated the NMO velocity from CMP gathers, where far-offsets tend to be more sensitive to velocity changes and the offset information is available. In our case, however, the information about the diffractor positions and the associated lateral distances of the interesting parts of the diffraction curves is not explicitly available, and we use attribute analysis to retrieve it. Diffraction-based migration velocity analyses provide the smooth large-scale velocity structure of the probed subsurface region, which is needed for

subsequent imaging and depth conversion. Liu et al. [17] recently illustrated how to combine this information with small-scale velocity fluctuations inferred from the reflected part of the GPR wavefield in order to obtain comprehensive estimates of the detailed velocity distribution. The diffraction velocity analysis component of the latter approach is likely to benefit from the corresponding improvements provided by the methods proposed in the current study. This is expected to be particularly pertinent in the presence of sub-optimal signal-to-noise ratios.

Arguably, the most important condition for a successful application of the proposed methodology is the presence of an ample amount of diffraction hyperbolae that are distributed reasonably evenly throughout the recorded common-offset GPR profile. Due to the inherent heterogeneity of the shallow subsurface, much of the incident GPR energy is indeed scattered/diffracted, rather than being reflected from specular interfaces [2], [14], meaning that this criterion is often satisfied. If such diffracted energy is missing along parts of the GPR profile, it was observed in our synthetic tests that the corresponding parts of the estimated velocity field will lose resolution. Another critical part of the proposed methodology is the effective isolation of the diffracted wavefield. In this study, standard PWD filtering was considered, but we expect that comparable results would be obtained through alternative approaches, such as, for example, coherent wavefield subtraction [22], [23]. In this regard, we have observed that much of the diffracted energy on a GPR section only becomes clearly visible after this step.

Although our weighting strategy contributes to increase the resolution of velocity spectra, there are still inherent uncertainties in the velocity picking process. For the automatic picking code ‘sfpick’, for example, two key input parameters required are the velocity at the surface and the smoothing radii in the horizontal and vertical directions, all of which have an effect on the results obtained [2]. Further, even with an optimal choice of these parameters, uncertainties remain in the obtained RMS velocity fields due to the sparse and/or uneven distribution of diffractors [2]. These uncertainties are, however, not specific to migration focusing analysis, and similarly prevail in all other types of diffraction-based velocity analysis techniques [7], [10]. The exploration, characterization, and quantification of these uncertainties is an important topic for future research. Another focus of future research will be the extension of the proposed technique from 2D to 3D, which is conceptually straightforward, but algorithmically cumbersome. This, in turn, is expected to significantly enhance the 3D migration velocity analysis of common-offset GPR data as, due to the inherent heterogeneity of the shallow subsurface, the diffracted energy present in corresponding 2D sections is likely to come from out-of-plane sources.

ACKNOWLEDGEMENTS

We are grateful to Yangkang Chen for inspiring discussions and thoughtful suggestions, which were tremendously helpful for getting this project started. We also thank the Madagascar development group for their open-source software, which we used for parts of this work.

REFERENCES

- [1] M. Grasmueck, R. Weger, and H. Horstmeyer, "Full-resolution 3D GPR imaging," *Geophysics*, vol. 70, no. 1, pp. 12–19, 2005, doi: 10.1190/1.1852780.
- [2] H. Yuan, M. Montazeri, M. C. Looms, and L. Nielsen, "Diffraction imaging of ground-penetrating radar data," *Geophysics*, vol. 84, no. 3, pp. H1–H12, 2019, doi: 10.1190/geo2018-0269.1.
- [3] W. S. Harlan, J. F. Claerbout, and F. Rocca, "Signal/noise separation and velocity estimation," *Geophysics*, vol. 49, no. 11, pp. 1869–1880, 1984.
- [4] S. Fomel, E. Landa, and M. T. Taner, "Poststack velocity analysis by separation and imaging of seismic diffractions," *Geophysics*, vol. 72, no. 6, pp. U89–U94, 2007, doi: 10.1190/1.2781533.
- [5] W. Burnett and S. Fomel, "Azimuthally anisotropic 3D velocity continuation," *Int. J. Geophys.*, vol. 2011, 2011, doi: 10.1155/2011/484653.
- [6] L. Decker, D. Merzlikin, and S. Fomel, "Diffraction imaging and time-migration velocity analysis using oriented velocity continuation," *Geophysics*, vol. 82, no. 2, pp. U25–U35, 2017, doi: 10.1190/geo2016-0141.1.
- [7] M. Reshef and E. Landa, "Post-stack velocity analysis in the dip-angle domain using diffractions," *Geophys. Prospect.*, vol. 57, no. 5, pp. 811–821, 2009, doi: 10.1111/j.1365-2478.2008.00773.x.
- [8] A. Klokov and S. Fomel, "Separation and imaging of seismic diffractions using migrated dip-angle gathers," *Geophysics*, vol. 77, no. 6, pp. S131–S143, 2012, doi: 10.1190/geo2012-0017.1.
- [9] E. Duvencek, "Velocity model estimation with data-derived wavefront attributes," *Geophysics*, vol. 69, no. 1, pp. 265–274, 2004, doi: 10.1190/1.1649394.
- [10] A. Bauer, B. Schwarz, and D. Gajewski, "Utilizing diffractions in wavefront tomography," *Geophysics*, vol. 82, no. 2, pp. R65–R73, 2017, doi: 10.1190/geo2016-0396.1.
- [11] J. Preine, B. Schwarz, A. Bauer, and C. Hübscher, "When There Is No Offset: A Demonstration of Seismic Diffraction Imaging and Depth-Velocity Model Building in the Southern Aegean Sea," *J. Geophys. Res. Solid Earth*, vol. 125, no. 9, pp. 1–19, 2020, doi: 10.1029/2020JB019961.
- [12] A. Novais, J. Costa, and J. Schleicher, "GPR velocity determination by image-wave remigration," *J. Appl. Geophys.*, vol. 65, no. 2, pp. 65–72, 2008, doi: 10.1016/j.jappgeo.2008.05.001.
- [13] J. S. Clair and W. S. Holbrook, "Measuring snow water equivalent from common-offset GPR records through migration velocity analysis," *Cryosphere*, vol. 11, no. 6, pp. 2997–3009, 2017, doi: 10.5194/tc-11-2997-2017.
- [14] H. Yuan, M. C. Looms, and L. Nielsen, "On the usage of diffractions in ground-penetrating radar reflection data: Implications for time-lapse gas migration monitoring," *Geophysics*, vol. 85, no. 5, pp. H83–H95, 2020, doi: 10.1190/geo2019-0343.1.
- [15] Z. Dong et al., "Properties analysis of lunar regolith at chang'E-4 landing site based on 3D velocity spectrum of lunar penetrating radar," *Remote Sens.*, vol. 12, no. 4, 2020, doi: 10.3390/rs12040629.
- [16] C. Li and J. Zhang, "Velocity analysis using separated diffractions for lunar penetrating radar obtained by yutu-2 rover," *Remote Sens.*, vol. 13, no. 7, 2021, doi: 10.3390/rs13071387.
- [17] Y. Liu, J. Irving, and K. Holliger, "High-resolution velocity estimation from surface-based common-offset GPR reflection data," *Geophys. J. Int.*, vol. 230, no. 1, pp. 131–144, 2022, doi: 10.1093/gji/ggac058.
- [18] S. Fomel, "Velocity analysis using AB semblance," *Geophys. Prospect.*, vol. 57, no. 3, pp. 311–321, 2009, doi: 10.1111/j.1365-2478.2008.00741.x.
- [19] M. T. Taner and F. Koehler, "Velocity spectra-digital computer derivation and applications of velocity functions," *Geophysics*, vol. 34, no. 6, pp. 859–881, 1969.
- [20] S. Luo and D. Hale, "Velocity analysis using weighted semblance," *Geophysics*, vol. 77, no. 2, pp. U15–U22, 2012, doi: 10.1190/geo2011-0034.1.
- [21] Y. Chen, T. Liu, and X. Chen, "Velocity analysis using similarity-weighted semblance," *Geophysics*, vol. 80, no. 4, pp. A75–A82, 2015, doi: 10.1190/geo2014-0618.1.
- [22] B. Schwarz and D. Gajewski, "Accessing the diffracted wavefield by coherent subtraction," *Geophys. J. Int.*, vol. 211, no. 1, pp. 45–49, 2017, doi: 10.1093/gji/ggx291.
- [23] B. Schwarz, "Coherent wavefield subtraction for diffraction separation," *Geophysics*, vol. 84, no. 3, pp. V157–V168, 2019, doi: 10.1190/geo2018-0368.1.
- [24] S. Fomel, "Applications of plane-wave destruction filters," *Geophysics*, vol. 67, no. 6, pp. 1946–1960, 2002, doi: 10.1190/1.1527095.
- [25] Z. Chen, S. Fomel, and W. Lu, "Accelerated plane-wave destruction," *Geophysics*, vol. 78, no. 1, pp. V1–V9, 2013, doi: 10.1190/geo2012-0142.1.
- [26] S. Fomel and A. Guitton, "Regularizing seismic inverse problems by model reparameterization using plane-wave construction," *Geophysics*, vol. 71, no. 5, pp. 43–47, 2006, doi: 10.1190/1.2335609.
- [27] C. Warren, A. Giannopoulos, and I. Giannakis, "gprMax: Open source software to simulate electromagnetic wave propagation for Ground Penetrating Radar," *Comput. Phys. Commun.*, vol. 209, pp. 163–170, 2016, doi: 10.1016/j.cpc.2016.08.020.
- [28] A. P. Annan, "Ground-Penetrating Radar," in *Near-Surface Geophysics*, Telsa, USA: Society of Exploration Geophysicists, 2005, ch.11, pp. 357–438, doi: 10.1190/1.9781560801719.ch11.
- [29] W. Barrash and T. Clemo, "Hierarchical geostatistics and multifacies systems: Boise Hydrogeophysical Research Site, Boise, Idaho," *Water Resour. Res.*, vol. 38, no. 10, pp. 14-1-14-18, 2002, doi: 10.1029/2002WR001436.
- [30] J. H. Bradford, W. P. Clement, and W. Barrash, "Estimating porosity with ground-penetrating radar reflection tomography: A controlled 3-D experiment at the Boise Hydrogeophysical Research Site," *Water Resour. Res.*, vol. 45, no. 4, pp. 1–11, 2009, doi: 10.1029/2008WR006960.
- [31] Z. Xu, J. Irving, Y. Liu, P. Zhu, and K. Holliger, "Conditional stochastic inversion of common-offset ground-penetrating radar reflection data," *Geophysics*, vol. 86, no. 5, pp. WB89–WB99, 2021, doi: 10.1190/geo2020-0639.1.
- [32] J. A. Huisman, S. S. Hubbard, J. D. Redman, and A. P. Annan, "Measuring Soil Water Content with Ground Penetrating Radar: A Review," *Vadose Zo. J.*, vol. 2, no. 4, pp. 476–491, Nov. 2003, doi: 10.2113/2.4.476.